Artificial intelligence-assisted magnetic resonance lymphography for evaluation of micro- and macro-sentinel lymph node metastasis in breast cancer

Zizhen Yang [a,1], Jianer Ling [a,1], Wei Sun [a], Chunshu Pan [a], Tianxiang Chen [b], Chen Dong [b], Xiaojun Zhou [a], Jingfeng Zhang [a,*], Jianjun Zheng [a,**], Xuehua Ma [b,***]

[a] *Department of Radiology, Ningbo No.2 Hospital, Ningbo, 315012, China*
[b] *Laboratory of Advanced Theranostic Materials and Technology, Ningbo Key Laboratory of Biomedical Imaging Probe Materials and Technology, Chinese Academy of Sciences (CAS) Key Laboratory of Magnetic Materials and Devices, Ningbo Institute of Materials Technology and Engineering, Chinese Academy of Sciences, Ningbo, 315201, China*

ARTICLE INFO

ABSTRACT

Contrast-enhanced magnetic resonance lymphography (CE-MRL) plays a crucial role in preoperative diagnostic for evaluating tumor metastatic sentinel lymph node (T-SLN), by integrating detailed lymphatic information about lymphatic anatomy and drainage function from MR images. However, the clinical gadolinium-based contrast agents for identifying T-SLN is seriously limited, owing to their small molecular structure and rapid diffusion into the bloodstream. Herein, we propose a novel albumin-modified manganese-based nanoprobes enhanced MRL method for accurately assessing micro- and macro-T-SLN. Specifically, the inherent concentration gradient of albumin between blood and interstitial fluid aids in the movement of nanoprobes into the lymphatic system. The micro-T-SLN exhibits a notably higher MR signal due to the formation of new lymphatic vessels and increased lymphatic flow, allowing for a greater influx of nanoprobes. In contrast, the macro-T-SLN shows a lower MR signal as a result of tumor cell proliferation and damage to the lymphatic vessels. Additionally, a highly accurate and sensitive machine learning model has been developed to guide the identification of micro- and macro-T-SLN by analyzing manganese-enhanced MR images. In conclusion, our research presents a novel comprehensive assessment framework utilizing albumin-modified manganese-based nanoprobes for a highly sensitive evaluation of micro- and macro-T-SLN in breast cancer.

1. Introduction

The accurate identification of micro- and macro-tumor metastatic sentinel lymph node (T-SLN) is crucial for predicting outcomes and planning treatment strategies for breast cancer [1–3]. Micro-T-SLN represents the early stage of tumor metastasis, which is important for evaluating lymph node involvement and deciding whether to perform an axillary lymph node dissection in breast cancer patients. Inversely, macro-T-SLN always indicates the further spread of tumor metastasis and a poor prognosis [4,5]. Consequently, the establishment of a highly sensitive and accurate diagnostic method is vital for efficient differentiation of micro- and macro-T-SLN in breast cancer patients.

In the clinic, the gold standard for detecting metastasis is the post-operative histological examination of lymph nodes. However, the invasive procedure can lead to complications such as chronic lymphatic insufficiency and lymphedema [6]. In recent years, non-invasive imaging techniques, including ultrasound (US), computed tomography (CT), magnetic resonance imaging (MRI), optical imaging, and radionuclide imaging, have become common in clinical assessments [7–10]. Radionuclide imaging is regarded as an effective technique for the diagnosis of lymphedema and can assist in intraoperative lymph node identification, but it poses challenges such as increased radiation exposure for both
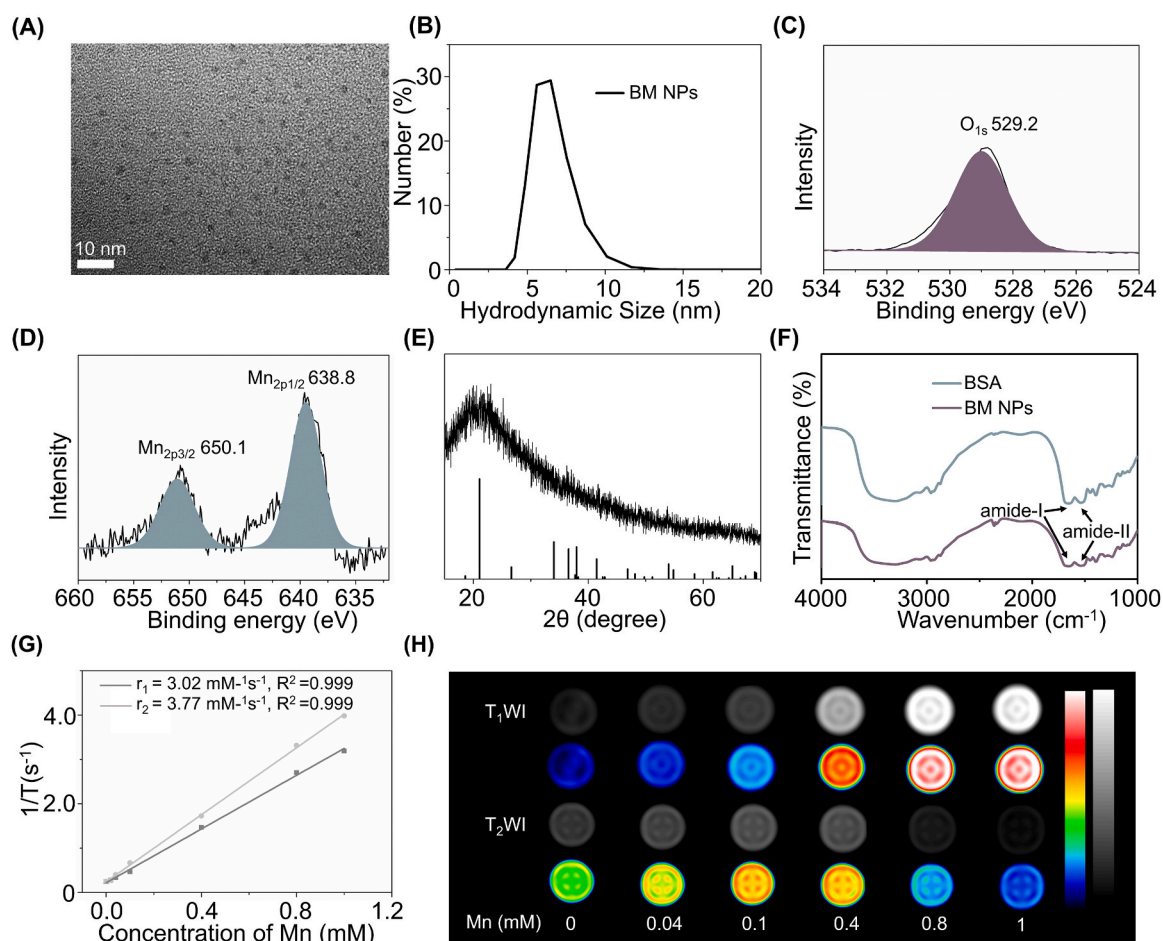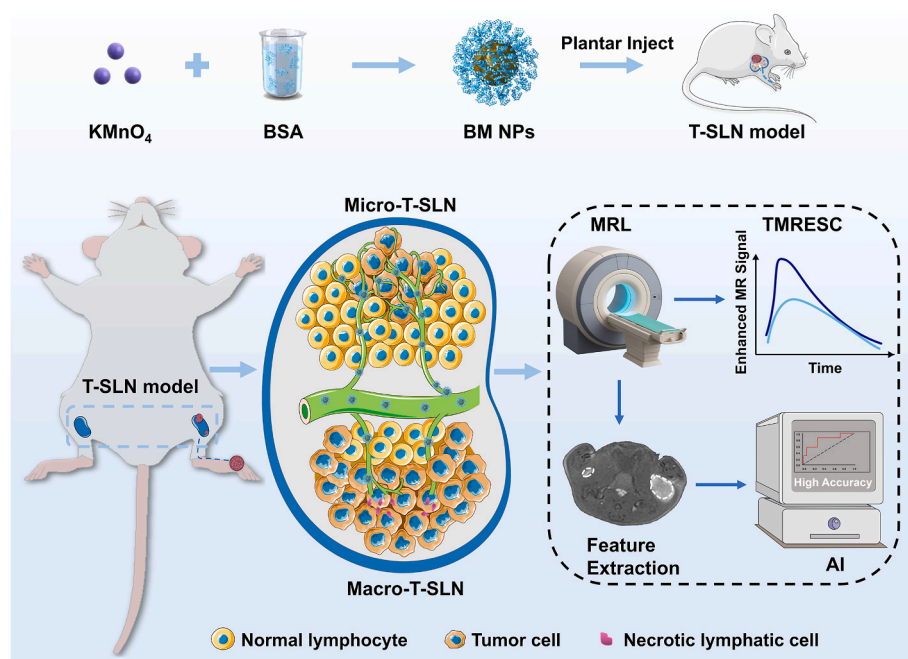

Scheme 1. Schematic illustration of the accurate evaluation of micro- and macro-T-SLN using Mn-enhanced MRL.

Fig. 1. (A) HRTEM images of BM NPs. (B) The hydrodynamic size of BM NPs. O element (C) and Mn element (D) of XPS pattern in BM NPs. (E) XRD pattern of BM NPs. (F) FTIR spectra of BSA, BM NPs. (G) Linear fitting of $1/T_1$ and $1/T_2$ of BM NPs in water with different Mn concentrations (0, 0.04, 0.1, 0.4, 0.8 and 1 mM). (H) Corresponding T_1/T_2-weighted and pseudo-color images of BM NPs. (For interpretation of the references to color in this figure legend, the reader is referred to the Web version of this article.)
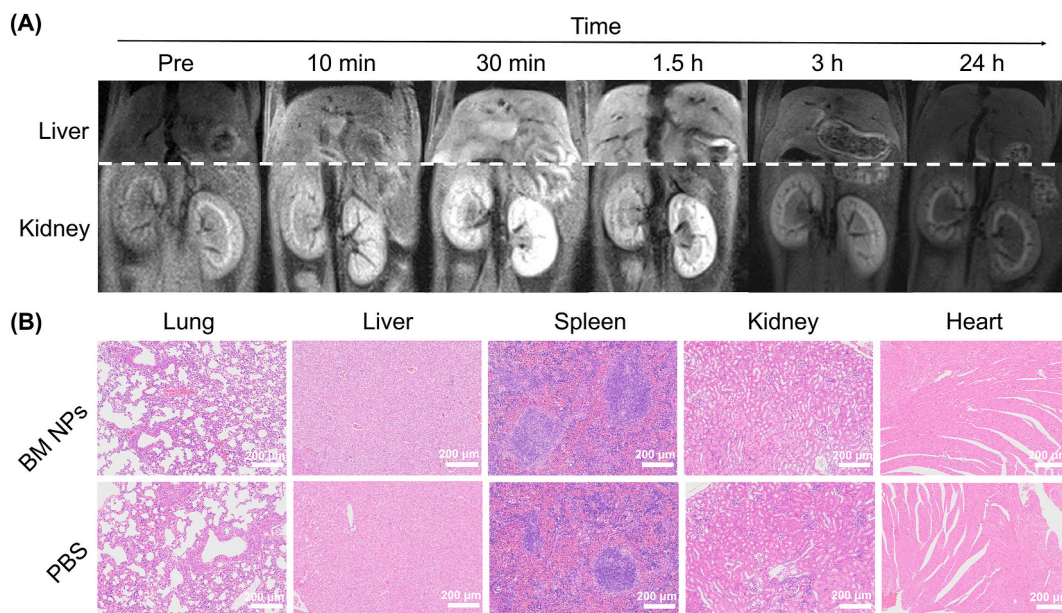
Fig. 2. (A) The metabolic behavior of BM NPs (18 mg/mL, 50 μL, n = 3) in vivo. (B) Histopathological results of main organs from mice 14 days after administration of BM NPs (18 mg/mL, 50 μL, n = 3).

patients and healthcare providers, limited anatomical detail, and high costs. On the other hand, optical imaging is frequently used during surgeries to locate sentinel lymph nodes due to its high sensitivity, affordability, and lack of radiation; however, it has drawbacks like poor optical penetration, low spatial resolution, potential contamination of surrounding tissues, and possible allergic reactions. Preoperative diagnostic staging of lymph nodes to inform surgical planning appears to be a more favorable approach. Currently, US, CT, and non-contrast MRI are commonly employed for preoperative assessments of lymph node metastasis, providing valuable anatomical information such as size and shape [11,12]. Nevertheless, US and CT have limitations, including low spatial resolution and the unavoidable radiation exposure associated with CT scans. While non-contrast MRI avoids radiation and offers better soft tissue contrast and spatial resolution compared to other methods, its effectiveness for lymph node staging remains limited.

Contrast-enhanced magnetic resonance lymphography (CE-MRL) involves the use of contrast agents in lymphatic vessels, providing detailed anatomical insights due to their high contrast and spatial resolution. Additionally, the contrast agents can indirectly indicate changes in lymphatic drainage function by monitoring their perfusion and metabolism [11]. This imaging capability positions CE-MRL as a promising diagnosis tool for accurate evaluation of T-SLN metastasis status. However, traditional gadolinium-based contrast agents (GBCAs) are not conducive for MRL because of their small molecular chelate structure that rapid diffusion into the bloodstream [13–15]. Furthermore, emerging clinical evidence has established an association between GBCAs administration and the pathogenesis of nephrogenic systemic fibrosis, with longitudinal studies demonstrating their propensity for chronic gadolinium deposition in renal-impaired patients [16,17]. To overcome the limitations of GBCAs, various MR contrast agents have been developed for CE-MRL, including magnetic nanoparticles [18–21], liposomes [22,23], polymeric compounds [24–26], and micelles [27–30], and so on [31]. While these contrast agents can effectively identify lymph node metastasis, challenges remain in differentiating between micro- and macro-T-SLN metastasis. Some superparamagnetic iron oxide (SPIO) nanoparticles, such as ferumoxtran-10, have received FDA approval as clinical T_2 contrast agents, but their negative signal complicates imaging in low MRI signal environments [20]. Manganese (Mn), an essential trace element, has shown promise as a basis for MR imaging probes, making them suitable for MRL and addressing the

limitations of GBCAs [32–35]. Although some Mn-based imaging probes have been effective in diagnosing T-SLN metastasis, distinguishing between micro- and macro-T-SLN metastasis still remains difficult [29]. Therefore, there is a pressing need to investigate effective MR contrast agents for the preoperative confirmation of both micro- and macro-T-SLN metastasis in breast cancer.

Albumin, the most prevalent protein in the bloodstream, exists in significantly higher concentrations in the blood compared to interstitial fluid (40 mg/mL vs. 14 mg/mL) [36,37]. This disparity in concentration tends to direct albumin toward the lymphatics system rather than blood capillaries [38–41]. Consequently, we developed a Mn-based nanoprobe that had been altered with albumin (bovine serum albumin-manganese dioxide nanoprobes, BM NPs), effectively and accurately identifying micro- and macro-T-SLN for the first time utilizing the contrast-enhanced MRL technique (Scheme 1). As a proof of concept, the biocompatible BM NPs were utilized for MRL in a mouse model with T-SLN metastasis, successfully capturing differential structural MR images of both micro- and macro-T-SLN. Additionally, by integrating various quantitative parameters related to lymphatic drainage function obtained from the images, such as peak value and relative lymph node clearance rate at 3 h (%RLC), we proposed a standardized framework to assess the metastasis status of T-SLN. The pathological analysis results confirmed the framework can accurately reflect the metastatic statuses of T-SLN (both micro- and macro-metastasis). Furthermore, an artificial intelligence (AI) method with high accuracy was built in our evaluation system, which can provide an efficient guidance for the assessment of micro- and macro-T-SLN [42–44].

2. Materials and methods

2.1. Materials and reagents

All chemicals and reagents used in this work were of at least analytical grade. Bovine serum albumin (BSA) was purchased from Beijing Dingguo Biotechnology Co., Ltd. (Beijing, China). Potassium permanganate ($KMnO_4$) was obtained from Sinopharm Chemical Reagent Co., Ltd. (Shanghai, China). Dulbecco's Modified Eagle Medium (DMEM) was sourced from Thermo Fisher Scientific Co., Ltd. (Suzhou, China). Methyl thiazolyl tetrazolium (MTT) was supplied by Shanghai Aladdin Reagent Co., Ltd. (Shanghai, China). Ultra-pure water
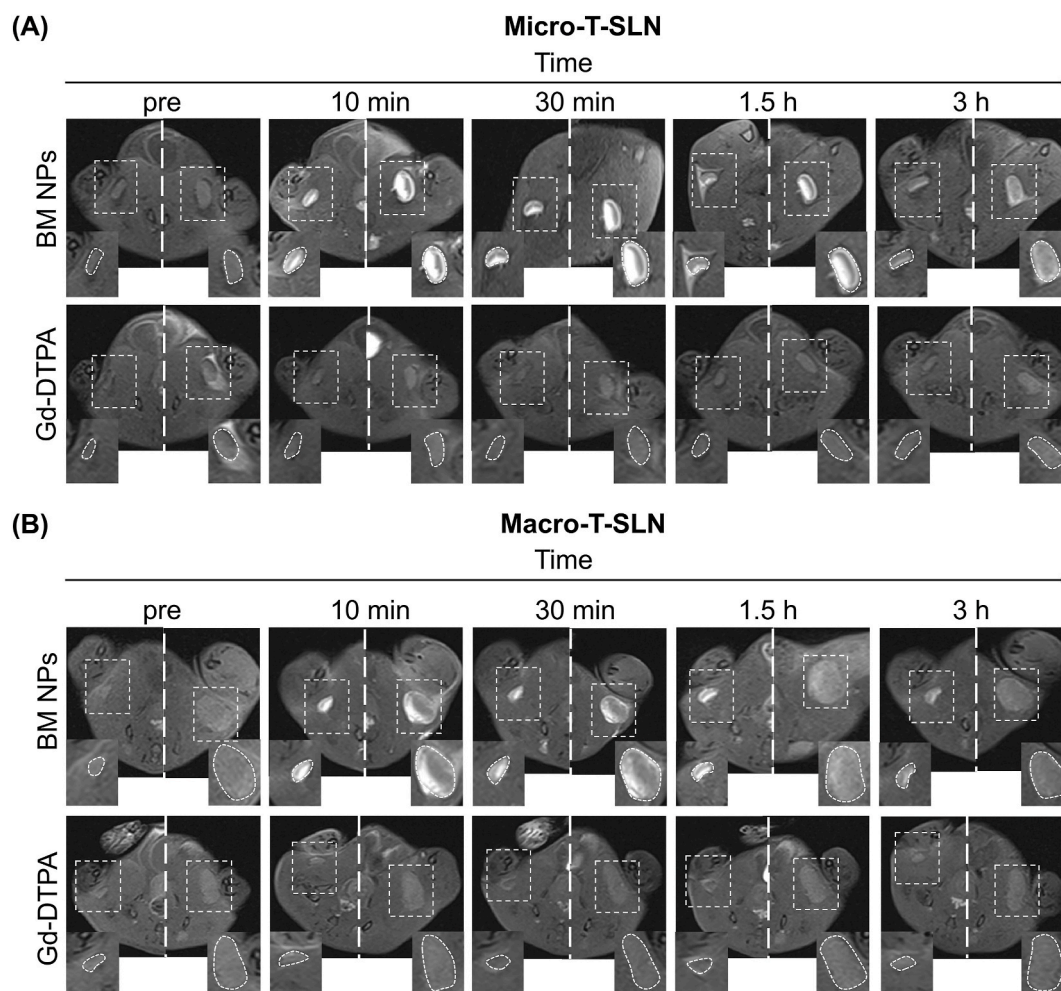
Fig. 3. (A) T_1-weighted MR images of micro-T-SLN mice were taken before and after plantar injection of BM NPs (n = 5) or Gd-DTPA (n = 3) at various time points (10 min, 30 min, 1.5 h, and 3 h). (B) T_1-weighted MR images of macro-T-SLN mice were taken before and after plantar injection of BM NPs (n = 5) or Gd-DTPA (n = 3) at various time points (10 min, 30 min, 1.5 h, and 3 h). Coronal section images of the largest left and right sentinel nodes at each time point were combined using separator lines (white dotted) to facilitate observation and comparison. In this context, T-SLN refers to tumor metastatic sentinel lymph node, while N-LN indicates normal sentinel lymph node.

(Millipore) was utilized to prepare all solutions in this study.

2.2. Characterization

The morphology and size of the nanoparticles were characterized using high-resolution transmission electron microscopy (HRTEM, Philips Tecnai G2 F20, Eindhoven, Netherlands). The core-level spectra and binding energies of the nanoparticles were recorded through X-ray photoelectron spectroscopy (XPS) measurements (Kratos Analytical Ltd., Manchester, England). Fourier transform infrared (FTIR) spectra (ranging from 650 to 4000 cm^{-1}) of the nanoparticles were obtained using a Nicolet IR AVATAR-360 spectrometer (Nicolet, Waltham, MA, USA) with pure KBr as background. The zeta potential and dynamic light scattering (DLS) of the nanoprobes were determined with a Malvern Zetasizer (Nano series ZS, Worcestershire, UK). The content of Mn element in BM NPs was measured using a Hitachi 180-80 atomic absorption spectrometer (Hitachi Co., Tokyo, Japan). The T_1/T_2 relaxivity (r_1/r_2) of BM NPs was acquired through T_1/T_2 mapping sequences from a 1.5 T MR scanner (Philips Healthcare, the Netherlands) with varying Mn concentrations (0, 0.04, 0.1, 0.4, 0.8 and 1 mM). In vitro T_1/T_2-weighted imaging of BM NPs was conducted following the scanning parameters: spin-echo sequence, T_1: TR = 600 ms, TE = 6.47 ms, T_2: TR = 2000 ms, TE = 104 ms (1.5 T MR scanner, Philips Healthcare, the Netherlands).

2.3. Synthesis of BM NPs

The BM NPs were synthesized using a previously established method [34,35]. Briefly, 31.6 mg of KMnO$_4$ was dispersed in 3 mL ultrapure water that was gradually added dropwise to 250 mg of BSA dispersed in 7 mL ultrapure water. Over time, the initially colorless solution transformed into a dark brown. The entire reaction was conducted under magnetic stirring at 37 °C for 2 h. The resulting BM NPs were purified by dialysis using the dialysis bag with a molecular weight cut-off of 8–14 kDa against water. Subsequently, the purified nanoparticles were freeze-dried and stored at 4 °C for future use.

2.4. Long-term colloidal stability of BM NPs

For the observation of long-term colloidal stabilization, 1 mg/mL of BM NPs were dispersed in water, phosphate buffer solution (PBS, 10 mM, pH = 7.4), normal saline, DMEM, and FBS, respectively. The photos were then taken to monitor the colloidal stability for 14 days.

2.5. Cell culture

4T1 cells were regularly cultured in a culture medium with 90 % 1640 and 10 % fetal bovine serum (FBS, Gibco, USA) in an atmosphere of 5 % CO$_2$ at 37 °C and the culture medium was refreshed at 1–2 days
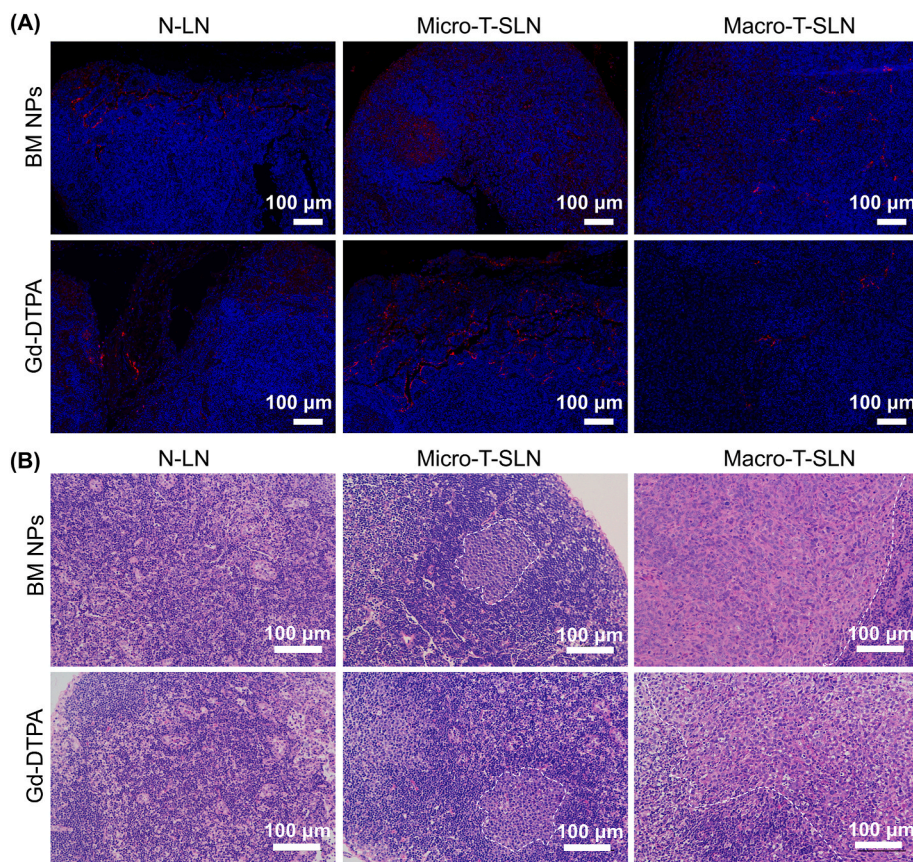
Fig. 4. (A) Double immunofluorescence staining images of the N-LN, micro- and macro-T-SLN in both BM NPs and Gd-DTPA group [LYVE-1–positive lymphatic vessels (red), 4', 6-diamidino-2-phenylindole (DAPI) staining for cell nuclei (blue)]. In this context, T-SLN refers to tumor metastatic sentinel lymph node, while N-LN indicates normal sentinel lymph node. (B) H&E staining images of the N-LN, micro- and macro-T-SLN in both BM NPs and Gd-DTPA group. (For interpretation of the references to color in this figure legend, the reader is referred to the Web version of this article.)

intervals.

2.6. In vitro cytotoxicity assay of BM NPs

To assess the potential cytotoxic effects of the BM NPs, 4T1 cells were seeded into 96-well plates in 200 μL of cell culture medium. After 24 h, the cells were incubated with fresh medium containing BM NPs at various concentrations (0, 10, 25, 50, 100, 200, 400, 800, and 1000 μg/mL) or PBS as control. After 24 h of incubation, cell viability was evaluated using a standard MTT assay. Briefly, after treatment with MTT (10 μL, 5 mg/mL) for 4 h, 120 μL DMSO was added to each well, and the absorbance of the solution was measured using a multimode microplate reader.

2.7. Establishment of tumor metastatic sentinel node (T-SLN) model

BALB/c mice (18–20 g, 6 weeks) were purchased from Hangzhou Muhao Biotechnology Co., Ltd. (Hangzhou, China). All animal experiments were conducted following protocols established by the ethics committee of the Guoke Ningbo Life Science and Health Industry Research Institute. To generate the T-SLN model, 4T1 cells (1×10^5 cells in 50 μL of PBS) were intraplantarly injected into the right leg of the BALB/c mice. Tissue sections were analyzed to confirm the T-SLN metastasis status. In our study, the Rotterdam criteria were utilized, where micro-T-SLN is defined as having a maximum tumor burden of 0.1–1 mm in diameter, and macro-T-SLN is defined as having a maximum tumor burden of >1 mm in diameter) [18,45].

2.8. CE-MRL of T-SLN model in vivo

To explore whether noninvasive MR imaging with BM NPs could facilitate the accurate diagnosis of T-SLN metastasis status, BM NPs or gadopentetic acid (Gd-DTPA) solution were injected into metastatic mice via plantar injection. T_1-weighted MR images were then acquired using a 3T MR scanner (Siemens, MAGNETOM Skyra 3.0 T) before the injection and at 10 min, 30 min, 1.5 h, and 3 h after plantar injection of either BM NPs (50 μL, containing 13.4 mmol/L of Mn atom as determined by ICP-MS, n = 5) or Gd-DTPA solution (50 μL, containing 13.4 mmol/L of gadolinium atom, n = 3). The scanning parameters were as follows: TR = 345 ms, TE = 13 ms, slice thickness = 1 mm, and FOV of 40 mm. The SLN specimens were collected following imaging experiments.

2.9. Image analysis

The MR images were acquired at various time points before and after the injection of BM NPs in T-SLN model mice. The bilateral sentinel lymph nodes from the largest coronal section images at the same time point were pieced to compile accurate observation and comparison. The MR signal values from the regions of interest (ROIs) of sentinel lymph nodes were recorded from the largest MR cross-sectional images. The enhancement signal (MES) was calculated by subtracting the MR value before the injection of BM NPs from the MR value after the injection of BM NPs. The MES values were then utilized to plot the time-dependent MR signal intensity curves (TMRESCs).

The parameters, including peak value and relative lymph node clearance rate (%RLC) at 3 h, were extracted from TMRESCs. If two
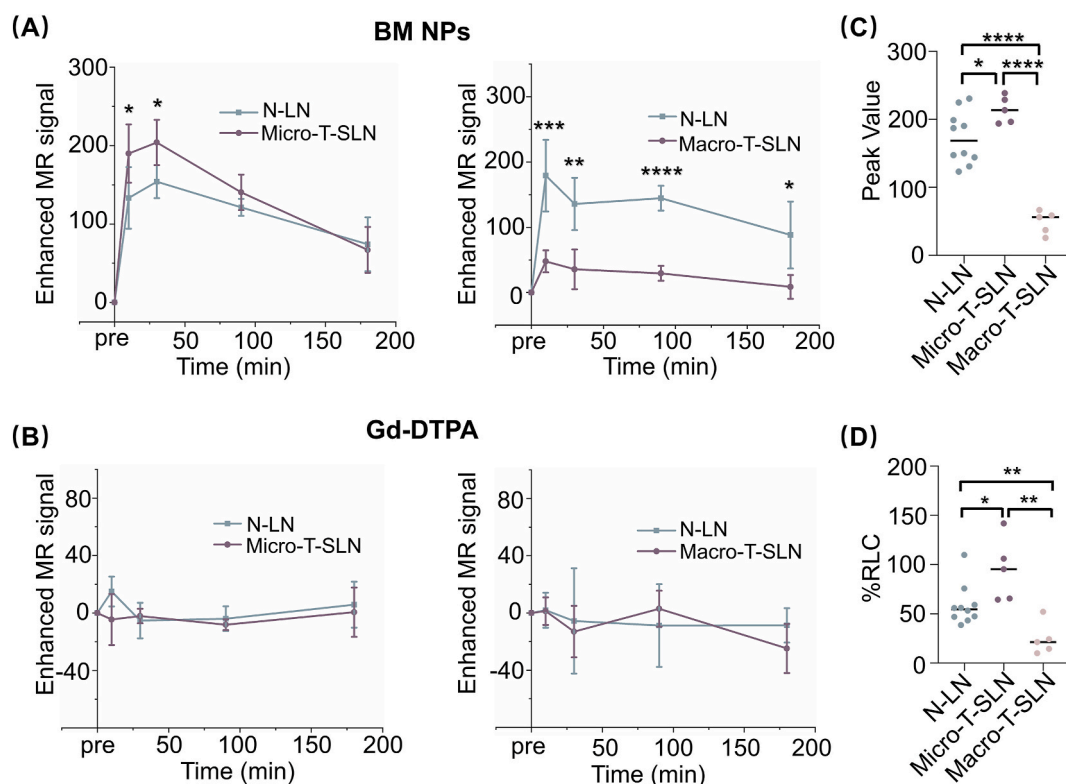
Fig. 5. The time-dependent enhanced MR signal curves of N-LN, micro- and macro-T-SLN after treatment with BM NPs (A, n = 5) or Gd-DTPA (B, n = 3). Statistical analysis of the Mn-enhanced T_1-weighted MR imaging of N-LN, micro- and macro-T-SLN by peak value (C) and %RLC (D). *$p < 0.05$, **$p < 0.01$, ***$p < 0.001$, ****$p < 0.0001$.

closely located peaks were present, the peak value of the first peak was designated as "peak value". The relevant calculation formula was as follows:

%RLC at 3 h = [(peak value – MES at 3 h) / peak value] × 100 %.

2.10. Pathological analysis

The sentinel lymph nodes were removed from the mice after completing the imaging experiments and were stored in 4 % para-formaldehyde. The tissue sections of the sentinel node were stained with hematoxylin and eosin (H&E).

2.11. In vivo toxicity of BM NPs

To further investigate the long-term biocompatibility of BM NPs in vivo, mice were treated with a BM solution (18 mg/mL, 50 μL) or 0.9 % saline (50 μL) as a control via plantar injection (n = 3). Then the blood was collected, and major organs (i.e., heart, lung, spleen, liver, and kidney) were excised for biochemical analysis and histological examination 14 days post-injection. The biochemical indicators primarily assessed included liver function markers (alanine aminotransferase-ALT, aspartate aminotransferase-AST, and total bilirubin-TBIL) and kidney function markers (creatinine-CREA, uric acid-UA, and urea). The weight of the mice was also monitored every two days until the 14th day.

2.12. Statistical analysis

All data were presented as the means ± standard deviation (SD). Comparison between groups were analyzed using two-tailed t-tests. A p-value of <0.05 is considered statistically significant, while a p-value of

<0.01 indicates a statistically highly significant.

3. Results and discussion

3.1. Synthesis and characterization of BM NPs

BM NPs were fabricated based on a drug-substrate mimic strategy according to our previous work (Fig. 1) [34,35]. Briefly, $KMnO_4$ (31.6 mg) dispersed in 3 mL of ultra-pure water was added dropwise into the BSA aqueous solution (250 mg of BSA, 7 mL), and the whole reaction was stirred magnetically for 2 h at 37 °C. During the process of this reaction, the colorless solution turned brown as soon as $KMnO_4$ was added, which means the formation of BM NPs through a redox reaction between $KMnO_4$ and BSA, with BSA acting as both the reductant and template. This method offers several advantages, including a straight-forward process, low cost, mild reaction conditions, and savings in time and energy.

HRTEM images showed the prepared BM NPs had a uniform size of 2.3 nm with a sphere shape and good uniformity (Fig. 1A, Fig. S1). The hydrodynamic size and zeta potential of the BM NPs were determined as 6.4 nm and −4.82 mV, respectively (Fig. 1B). XPS examined the composition of the nanoparticles. Fig. 1C and D showed that the XPS spectra confirmed the existence of O and Mn elements, with three peaks centered at 529.2, 642.5, and 654.0 eV corresponding to O_{1s}, $Mn_{2p3/2}$, and $Mn_{2p1/2}$ of MnO_2, respectively. The X-ray Diffraction (XRD) pattern of the BM NPs displayed distinct peaks at $2\theta = 21.06°$ using the Rigaku Ultima IV diffractometer with a temperature chamber operating at 40 kV/20 mA, consistent with the characteristic peaks of MnO_2 (Fig. 1E) [34]. Additionally, a strong absorption band in the range of 300–400 nm was attributed to the plasmonic absorption of MnO_2, indicating its for-mation (Fig. S2) [35]. The presence of protein residues was further validated by FTIR spectroscopy. As shown in Fig. 1F, the typical ab-sorption bands at 1655 cm^{-1} for amide-I, and 1540 cm^{-1} for amide-II in
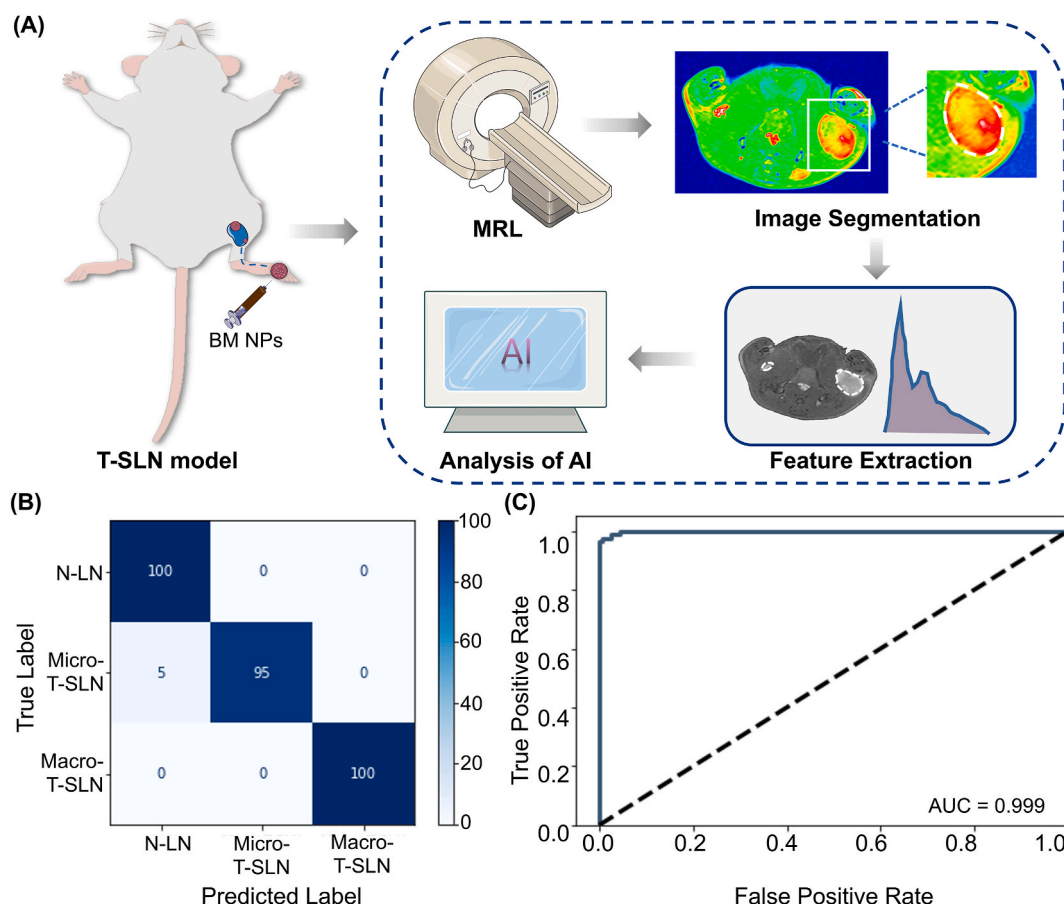
Fig. 6. (A) Schematic diagram of artificial intelligence for guiding the diagnosis of T-SLN. (B) ROC analysis of N-LN, micro- and macro-T-SLN. (C) Confusion matrix for 3 strain classes. n = 5 for each group. Mean values are given.

BSA, indicated abundant BSA in the BM NPs. Furthermore, the Mn element content in the BM NPs was determined to be 4.1 % according to Inductively Coupled Plasma Atomic Emission Spectroscopy (ICP-AES) analysis.

To evaluate the colloidal stability, BM NPs were dispersed in various media, including pure water, PBS at pH = 7.4, 0.9 % normal saline, DMEM, and serum. No precipitation was observed in any of these solutions over 14 days, demonstrating the excellent solubility and long-term stability of the BM NPs (Fig. S3). Additionally, to evaluate their MR imaging capabilities, the T_1/T_2 relaxivity of the BM NPs was measured, and in vitro T_1/T_2-weighted imaging was conducted using a 1.5 T MR scanner. The r_1 and r_2 values of the BM NPs were determined to be 3.02 mM^{-1} s^{-1} and 3.77 mM^{-1} s^{-1}, respectively (Fig. 1G). As shown in Fig. 1H, the T_1-weighted signal intensity of the BM NPs increased in a concentration-dependent manner, while there was a T_2-weighted signal decreasing with the increasing concentration of the BM NPs. These results indicated that the BM NPs possessed small and uniform size, excellent colloidal stability, and remarkable MR imaging capabilities.

3.2. Metabolic behavior of BM NPs in vivo

To further investigate the metabolic biodistribution of BM NPs in vivo, MR imaging was performed on normal mice using a 3T MR scanner after plantar injection of BM NPs (18 mg/mL, 50 μL, n = 3). As shown in Fig. 2A, the liver and kidneys exhibited an immediate increase in brightness after the administration of BM NPs. The peak MR signal intensity was observed 30 min after plantar injection, with significantly increased MR signals in the liver and kidney lasting approximately 1.5 h. Thereafter, the BM NPs began to be metabolized gradually, and by 24 h, the signals from the liver and kidney had nearly returned to baseline

levels.

3.3. Toxicity assessment of BM NPs in vitro and in vivo

The standard cellular MTT assay was employed to evaluate the cytotoxicity of BM NPs. The viability of 4T1 cells showed no significant variation within the concentration range from 0 to 1000 μg/mL BM NPs. Even at the concentration up to 1000 μg/mL, the viability of 4T1 cells still remained over 90 % (Fig. S4A). These results demonstrated that the BM NPs exhibited low cytotoxicity.

To further investigate the in vivo toxicity of BM NPs, a thorough examination was conducted on blood biochemical tests, histopathologic analyses, and body weight changes of mice after the BM NPs treatment. The biochemical markers for liver function (alanine aminotransferase-ALT, aspartate aminotransferase-AST, and total bilirubin-TBIL) and kidney function (creatinine-CREA, uric acid-UA, and urea) in the experimental group showed no significant differences compared to the control group (Fig. S4C). The histopathological results showed no obvious histological alteration in the main organs (heart, liver, spleen, lung, and kidney) after the injection of BM NPs (Fig. 2B). Additionally, there were no abnormal changes in body weight among the mice during a 14-day period after BM NPs administration when compared to the control group (Fig. S4B). Overall, these results demonstrated that the BM NPs exhibited excellent biocompatibility in vivo.

3.4. CE-MRL of BM NPs in T-SLN model

To explore the diagnostic potential of BM-based noninvasive MR imaging in determining the metastasis status of T-SLNs, we developed a T-SLN model for micro-metastasis (0.1 mm < d ≤ 1 mm) and macro-

metastasis (d > 1 mm). This was achieved by intracutaneous injection of 4T1 cells into the right leg of BALB/c mice [18,45]. After plantar injection of the BM NPs and Gd-DTPA, T_1-weighted images of both micro- and macro-T-SLN models were captured at various time points (n = 5). It can be found that there was no significant MR signal changes were observed before and after the administration of Gd-DTPA both in micro- and macro-T-SLN model mice (the lower row in Fig. 3A and B) [13–15]. The possible reasons were related to the small molecular size of Gd-DTPA that rapidly diffused into the bloodstream without entering lymph node [13–15]. Following the administration of BM NPs, the MR signals of both micro- and macro-T-SLN were significantly enhanced, suggesting that the BM NPs were engulfed by lymph node. As we anticipated, the natural concentration gradient of albumin between blood and interstitial fluid caused the BM NPs to preferentially move towards the lymphatics system instead of the blood capillaries, which in turn supported the application of Mn-enhanced MRL in the T-SLN model [38–41]. However, at the same time point, the MR enhancement of micro-T-SLN exhibited significant heterogeneity compared to macro-T-SLN, being higher than that of macro-T-SLN. Additionally, the boundaries of micro-T-SLN became clearer 10 min after the injection of BM NPs, with enhancement lasting for 1.5 h before weakening after 3 h. In contrast, macro-T-SLN displayed clear boundaries after 10 min of injection, but the enhancement persisted for only 30 min and began to weaken after 1.5 h (upper row in Fig. 3A and B). Structurally, the right T-SLN was larger than the adjacent normal sentinel lymph node (N-LN), particularly in the macro-T-SLN model, which aligned with the images of excised N-LN, as well as micro- and macro-T-SLN (Fig. S5). Consequently, it was possible to distinguish between micro- and macro-T-SLN by monitoring changes in MR signals.

We hypothesized that a significantly higher MR signal in micro-T-SLN compared to N-LN and macro-T-SLN resulted from the tissue remodeling of SLN during the early stages of metastasis, which facilitated a greater influx of BM NPs into the micro-T-SLN. Furthermore, additional immunofluorescence staining of lymphatic vessels was conducted to confirm the presence of lymphatic vessels in both micro- and macro-T-SLN, as well as in N-LN. As shown in Fig. 4A, a higher fluorescence intensity of lymphatic vessel endothelial receptor (LYVE)-1-positive lymphatic vessels in the micro-T-SLN compared to N-LN and macro-T-SLN, indicated an increasing lymph angiogenesis in the micro-T-SLN. Owing to the further proliferation of tumor cells and destruction of lymphatic vessels, the fluorescence intensity of LYVE-1-positive lymphatic vessels significantly declined in the macro-T-SLN. The results from the immunofluorescence staining analysis further aligned with our hypothesis. Additionally, histopathologic analysis using H&E staining of T-SLN illustrated that the N-LN exhibited deep nucleus staining and a uniform shape, while the T-SLN contained tumor cells with large, abnormal nuclei (Fig. 4B). The findings indicated that T-SLN models incorporating various transition statuses had been effectively created, demonstrating their efficacy in diagnosing both micro- and macro-T-SLN.

3.5. Quantitative MR imaging analysis

To evaluate the T-SLN metastasis status quantitatively, we analyzed TMRESCs extracted from MR images. As illustrated in Fig. 5A, the MR signal for T-SLN was stronger than that of N-LN at various time points in mice with micro-T-SLN. Conversely, in mice with macro-T-SLN, the MR signal for T-SLN was weaker than that of N-LN at the same time points. TMRESCs presented in Fig. 5B indicated no significant difference before and after administration of Gd-DTPA in both micro- and macro-T-SLN metastatic mice. The result of TMRESCs was consistent with the Mn-enhanced MR images. Additionally, we extracted two quantitative parameters (peak value and %RLC) from the TMRESCs to enhance the evaluation of T-SLN metastasis status. The peak value in micro-T-SLN showed a significant increase of 24.1 % (p < 0.05) when compared to the N-LN. Nevertheless, the peak values of macro-T-SLN decreased by

71.7 % (p < 0.0001) relative to the contralateral N-LN (Fig. 5C). The % RLC at 3 h is calculated as [(peak value – 3 h MR enhanced signal)/peak value] × 100 %. As illustrated in Fig. 5D, the %RLC at 3 h increased from 58.6 % in N-LN to 94.7 % in micro-T-SLN (p < 0.05) but declined to 24.4 % in macro-T-SLN (p < 0.01). These two quantitative parameters can offer additional insights for a detailed assessment of T-SLN metastatic status. According to Mn-enhanced MR images and the results of quantitative analysis of TMRESCs in micro- and macro-T-SLN models, we can accurately and effectively distinguish between micro- and macro-T-SLN, successfully achieving accurate diagnosis of T-SLN metastasis status via Mn-enhanced MRL.

Besides, we utilized an AI method to determine the T-SLN metastasis status by analyzing Mn-enhanced MR images. The performance of the AI model was assessed by a 10-fold cross-validation, and the results demonstrated that the AI model performed exceptionally well, achieving accuracy rates exceeding 90 %. The development of the protocol involved Mn-enhanced MRL, segmentation of the sentinel lymph node region, extraction of image features, and the creation of imaging signatures using a support vector machine (Fig. 6A). We calculated the receiver operating characteristic (ROC) curve to assess the accuracy of the diagnostic method, which was represented by the area under the curve (AUC). This graph is primarily plotted with the false positive rate (specificity) on the X-axis and the true positive rate (sensitivity) on the Y-axis. The AUC values were categorized into five levels: fail (AUC <0.50), poor (AUC 0.60–0.70), fair (AUC 0.70–0.80), good (AUC 0.80–0.90), and excellent (AUC 0.90–1.00). As shown in Fig. 6B, we achieved excellent accuracy in distinguishing T-SLN metastasis status using this AI method (AUC = 0.999). The identification accuracy reached 98.3 %, as indicated by the confusion matrix (Fig. 6C). When combined with Mn-based enhanced MRL, an AI method with high sensitivity and accuracy was developed to guide the differentiation of N-LN, micro- and macro-T-SLN.

4. Conclusions

In summary, we have developed an effective and accurate method for assessing the micro- and macro-T-SLN by integrating Mn-based enhanced MRL with AI for the first time. The synthesized BM NPs exhibited good solubility and stability in water. Moreover, toxicity evaluations showed no significant alterations in the structure of main organs or blood biochemical markers following the plantar injection of BM NPs, indicating their low toxicity. The natural difference in albumin concentration (40 mg/mL in blood compared to 14 mg/mL in the interstitial fluid) drove BM NPs more inclined to enter the lymphatics vessels rather than blood capillaries, provided high-contrast MRL images about lymphatic structural and functional information, including structural changes in lymph nodes, lymphatic drainage, and clearance capabilities. The formation of new lymphatic vessels and heightened lymphatic flow in micro-T-SLN allowed more BM NPs to enter into lymph node, which made a significantly higher MR signal in micro-T-SLN. Inversely, lymphatic vessels in macro-T-SLN were further destroyed due to proliferation of tumor cells, resulting in a lower MR signal. We analyzed the diagnostic data obtained and developed a novel framework for the accurate diagnosis of T-SLN metastasis status, which aligned with histopathological analysis. Additionally, a high-performance AI method further was involved in guidance for T-SLN metastatic diagnosis (AUC = 0.999). In a conclusion, our study demonstrates that BM-based enhanced MRL can be a promising and powerful tool for the high-accuracy diagnosis of T-SLN metastasis status. However, there are some limitations that the issue of false positives caused by inflammation or reactive hyperplastic lymphadenopathy is not fully involved in this work, which needs a follow-up study in the future.

CRediT authorship contribution statement

Zizhen Yang: Writing – original draft, Investigation, Funding

acquisition, Formal analysis, Data curation. **Jianer Ling:** Writing – original draft, Investigation, Formal analysis, Data curation. **Wei Sun:** Supervision, Data curation. **Chunshu Pan:** Supervision, Data curation. **Tianxiang Chen:** Supervision, Conceptualization. **Chen Dong:** Supervision, Conceptualization. **Xiaojun Zhou:** Supervision, Data curation. **Jingfeng Zhang:** Writing – review & editing, Validation, Supervision, Conceptualization. **Jianjun Zheng:** Writing – review & editing, Validation, Supervision, Funding acquisition, Conceptualization. **Xuehua Ma:** Writing – review & editing, Validation, Supervision, Conceptualization.

Declaration of competing interest

The authors declare that they have no known competing financial interests or personal relationships that could have appeared to influence the work reported in this paper.

Acknowledgments

Appendix A. Supplementary data

Supplementary data to this article can be found online at https://doi.org/10.1016/j.mtbio.2025.101692.

Data availability

Data will be made available on request.

References

[1] A.E. Giuliano, J.L. Connolly, S.B. Edge, E.A. Mittendorf, H.S. Rugo, L.J. Solin, D.L. Weaver, D.J. Winchester, G.N. Hortobagyi, Breast cancer-major changes in the American joint committee on cancer eighth edition cancer staging manual, CA Cancer J. Clin. 67 (2017) 291–303.

[2] S. Lukasiewicz, M. Czeczelewski, A. Forma, J. Baj, R. Sitarz, A. Stanislawek, Breast cancer-epidemiology, risk factors, classification, prognostic markers, and current treatment strategies-an updated review, Cancers 13 (2021) 4287.

[3] S.P.L. Leong, M. Zuber, R.L. Ferris, Y. Kitagawa, R. Cabanas, C. Levenback, M. Faries, S. Saha, Impact of nodal status and tumor burden in sentinel lymph nodes on the clinical outcomes of cancer patients, J. Surg. Oncol. 103 (2011) 518–530.

[4] K. Naidoo, S.E. Pinder, Micro- and macro-metastasis in the axillary lymph node: a review, Surg-J. R. Coll. Surg. E. 15 (2017) 76–82.

[5] G.J. Whitman, R.H. AlHalawani, N. Karbasian, R. Krishnamurthy, Sentinel lymph node evaluation: what the radiologist needs to know, Diagnostics 9 (2019) 12.

[6] N.A.C. Bakri, R.M. Kwasnicki, N. Khan, O. Ghandour, A. Lee, Y. Grant, A. Dawidziuk, A. Darzi, H. Ashrafian, D.R. Leff, Impact of axillary lymph node dissection and sentinel lymph node biopsy on upper limb morbidity in breast cancer patients a systematic review and meta-analysis, Ann. Surg. 277 (2023) 572–580.

[7] A.K. Polomska, S.T. Proulx, Imaging Technology of the lymphatic system, Adv. Drug Deliv. Rev. 170 (2021) 294–311.

[8] S.L. Qi, X.Y. Wang, K. Chang, W.B. Shen, G.C. Yu, J.S. Du, The bright future of nanotechnology in lymphatic system imaging and imaging-guided surgery, J. Nanobiotechnol. 20 (2022) 24.

[9] Z.Q. Cheng, J.J. Ma, L. Yin, L.Y. Yu, Z. Yuan, B. Zhang, J. Tian, Y. Du, Non-invasive molecular imaging for precision diagnosis of metastatic lymph nodes: opportunities from preclinical to clinical applications, Eur. J. Nucl. Med. Mol. Imag. 50 (2023) 1111–1133.

[10] V. Cuccurullo, M. Rapa, B. Catalfamo, G.L. Cascini, Role of nuclear sentinel lymph node mapping compared to new alternative imaging methods, J. Pers. Med. 13 (2023) 1219.

[11] M. Han, R.R. Kang, C.Q. Zhang, Lymph node mapping for tumor micrometastasis, ACS Biomater. Sci. Eng. 8 (2022) 2307–2320.

[12] B. Misselwitz, MR contrast agents in lymph node imaging, Eur. J. Radiol. 58 (2006) 375–382.

[13] H.B. Zhou, P.J. Lei, T.P. Padera, Progression of metastasis through lymphatic system, Cells 10 (2021) 627.

[14] L. Gillot, L. Baudin, L. Rouaud, F. Kridelka, A. Noël, The pre-metastatic niche in lymph nodes: formation and characteristics, Cell. Mol. Life Sci. 78 (2021) 5987–6002.

[15] Y. Chen, S. De Koker, B.G. De Geest, Engineering strategies for lymph node targeted immune activation, Acc. Chem. Res. 53 (2020) 2055–2067.

[16] M. Mathur, J.R. Jones, J.C. Weinreb, Gadolinium deposition and nephrogenic systemic fibrosis: a radiologist's primer, Radiographics 40 (2020) 153–162.

[17] N. Schieda, C.B. van der Pol, D. Walker, A.K. Tsampalieros, P.J. Maralani, S. Woo, M.S. Davenport, Adverse events to the gadolinium-based contrast agent gadoxetic acid: systematic review and meta-analysis, Radiology 297 (2020) 565–572.

[18] X.M. Fu, S.X. Fu, Z.Y. Cai, R.R. Jin, C.C. Xia, S. Lui, B. Song, Q.Y. Gong, H. Ai, Manganese porphyrin/ICG nanoparticles as magnetic resonance/fluorescent dual-mode probes for imaging of sentinel lymph node metastasis, J. Mater. Chem. B 10 (2022) 10065–10074.

[19] X.M. Fu, Z.Y. Cai, S.X. Fu, H.W. Cai, M.F. Li, H.J. Gu, R.R. Jin, C.C. Xia, S. Lui, B. Song, Q.Y. Gong, H. Ai, Porphyrin-based self-assembled nanoparticles for PET/MR imaging of sentinel lymph node metastasis, ACS Appl. Mater. Interfaces 16 (2024) 27139–27150.

[20] Y.L. Yan, Y.H. Liu, T.F. Li, Q.J. Liang, A. Thakur, K. Zhang, W. Liu, Z.J. Xu, Y.Z. Xu, Functional roles of magnetic nanoparticles for the identification of metastatic lymph nodes in cancer patients, J. Nanobiotechnol. 21 (2023) 337.

[21] G. Wang, W. Li, G. Shi, Y. Tian, L. Kong, N. Ding, J. Lei, Z. Jin, J. Tian, Y. Du, Sensitive and specific detection of breast cancer lymph node metastasis through dual-modality magnetic particle imaging and fluorescence molecular imaging: a preclinical evaluation, Eur. J. Nucl. Med. Mol. Imag. 49 (2022) 2723–2734.

[22] S. Hamaguchi, I. Tohnai, A. Ito, K. Mitsudo, T. Shigetomi, M. Ito, H. Honda, T. Kobayashi, M. Ueda, Selective hyperthermia using magnetoliposomes to target cervical lymph node metastasis in a rabbit tongue tumor model, Cancer Sci. 94 (2003) 834–839.

[23] J. Sheng, Y. Liu, H. Ding, L. Wu, L. Liu, G. Si, Y. Shen, F. Yang, N. Gu, Magnetic delivery of antigen-loaded magnetic liposomes for active lymph node targeting and enhanced anti-tumor immunity, Adv. Healthcare Mater. 12 (2023) e2301232.

[24] M. Muthiah, H. Vu-Quang, Y.K. Kim, J.H. Rhee, S.H. Kang, S.Y. Jun, Y.J. Choi, Y.Y. Jeong, C.S. Cho, I.K. Park, Mannose-poly(ethylene glycol)-linked SPION targeted to antigen presenting cells for magnetic resonance imaging on lymph node, Carbohydr. Polym. 92 (2013) 1586–1595.

[25] Y. Zhan, W. Zhan, H. Li, X. Xu, X. Cao, S. Zhu, J. Liang, X. Chen, In vivo dual-modality fluorescence and magnetic resonance imaging-guided lymph node mapping with good biocompatibility manganese oxide nanoparticles, Molecules 22 (2017) 2208.

[26] Y. Nie, Y. Rui, C. Miao, Q. Li, F. Hu, H. Gu, A stable USPIO capable for MR lymphography with ultra-low effective dosage, Nanomedicine 29 (2020) 102233.

[27] V.S. Trubetskoy, M.D. Frank-Kamenetsky, K.R. Whiteman, G.L. Wolf, V.P. Torchilin, Stable polymeric micelles: lymphangiographic contrast media for gamma scintigraphy and magnetic resonance imaging, Acad. Radiol. 3 (1996) 232–238.

[28] Y. Jiang, Z. Cai, S. Fu, H. Gu, X. Fu, J. Zhu, Y. Ke, H. Jiang, W. Cao, C. Wu, C. Xia, S. Lui, B. Song, Q. Gong, H. Ai, Relaxivity enhancement of hybrid micelles via modulation of water coordination numbers for magnetic resonance lymphography, Nano Lett. 23 (2023) 8505–8514.

[29] H. Akai, K. Shiraishi, M. Yokoyama, K. Yasaka, M. Nojima, Y. Inoue, O. Abe, K. Ohtomo, S. Kiryu, PEG-poly(L-lysine)-based polymeric micelle MRI contrast agent: feasibility study of a Gd-micelle contrast agent for MR lymphography, J. Magn. Reson. Imag. 47 (2018) 238–245.

[30] K. Chen, Z.Y. Cai, Y.Z. Cao, L.L. Jiang, Y.T. Jiang, H.J. Gu, S.X. Fu, C.C. Xia, S. Lui, Q.Y. Gong, B. Song, H. Ai, Kinetically inert manganese (II)-Based hybrid micellar complexes for magnetic resonance imaging of lymph node metastasis, Regen. Biomater. 10 (2023) rbad053.

[31] H.R. Lan, Y.N. Zhang, Y.J. Han, S.Y. Yao, M.X. Yang, X.G. Xu, X.Z. Mou, K.T. Jin, Multifunctional nanocarriers for targeted drug delivery and diagnostic applications of lymph nodes metastasis: a review of recent trends and future perspectives, J. Nanobiotechnol. 21 (2023) 247.

[32] E.M. Gale, I.P. Atanasova, F. Blasi, I. Ay, P. Caravan, A manganese alternative to gadolinium for MRI contrast, J. Am. Chem. Soc. 137 (2015) 15548–15557.

[33] L. Zhou, Z.Z. Yang, L. Guo, Q. Zou, H. Zhang, S.K. Sun, Z.X. Ye, C. Zhang, Noninvasive assessment of kidney injury by combining structure and function using artificial intelligence-based manganese-enhanced magnetic resonance imaging, ACS Appl. Mater. Interfaces 16 (2024) 5474–5485.

[34] J. Pan, Y. Wang, H. Pan, C. Zhang, X. Zhang, Y.-Y. Fu, X. Zhang, C. Yu, S.-K. Sun, X.-P. Yan, Mimicking drug-substrate interaction: a smart bioinspired Technology for the fabrication of theranostic nanoprobes, Adv. Funct. Mater. 27 (2017) 1603440.

[35] W.J. Hou, Y.Z. Jiang, G.C. Xie, L. Zhao, F.S. Zhao, X.J. Zhang, S.K. Sun, C.S. Yu, J.B. Pan, Biocompatible BSA-MnO$_2$ nanoparticles for in vivo timely permeability imaging of blood-brain barrier and prediction of hemorrhage transformation in acute ischemic stroke, Nanoscale 13 (2021) 8531–8542.

[36] E.N. Hoogenboezem, C.L. Duvall, Harnessing albumin as a carrier for cancer therapies, Adv. Drug Deliv. Rev. 130 (2018) 73–89.

[37] J. De Vrieze, B. Louage, K. Deswarte, Z.F. Zhong, R. De Coen, S. Van Herck, L. Nuhn, C.K. Frich, A.N. Zelikin, S. Lienenklaus, N.N. Sanders, B.N. Lambrecht, S. A. David, B.G. De Geest, Potent lymphatic translocation and spatial control over innate immune activation by polymer-lipid amphiphile conjugates of small-molecule TLR7/8 agonists, Angew. Chem., Int. Ed. 58 (2019) 15390–15395.

[38] T.T. Song, Y.F. Xia, Y.Q. Du, M.W. Chen, H. Qing, G.H. Ma, Engineering the deformability of albumin-stabilized emulsions for lymph-node vaccine delivery, Adv. Mater. 33 (2021) 2100106.

[39] X.H. Wang, D. Chen, K.X. Huang, M. Li, C.Y. Zhan, Z.Y. Dong, T. Deng, K.B. Ren, Y. Qiu, Z.R. Zhang, Q. He, Albumin-hitchhiking drug delivery to tumor-draining lymph nodes precisely boosts tumor-specific immunity through autophagy modulation of immune cells, Adv. Mater. 35 (2023) 2211055.

[40] Q. Wang, Q.K. Jiang, D. Li, C. Li, Y. Feng, Z.M. Yang, Z.G. He, C. Luo, J. Sun, Self-adaptive non-covalent albumin-binding near-infrared probe conjugates enabling precise sentinel lymph node metastasis illumination and primary tumor imaging, Nano Res. 16 (2023) 3010–3020.

[41] H. Iqbal, A. Razzaq, F. Liu, F.R. Zhang, J. Tao, T. Li, Y.Q. Jiang, Z.D. Zhao, M. T. Qin, X.H. Lin, H.T. Ke, H.B. Chen, Y.B. Deng, A bioinspired doxorubicin-carried albumin nanocage against aggressive cancer via systemic targeting of tumor and lymph node metastasis, J. Contr. Release 372 (2024) 829–845.

[42] Y.L. Balachandran, W. Wang, H.Y. Yang, H.Y. Tong, L.L. Wang, F. Liu, H.S. Chen, K. Zhong, Y. Liu, X.Y. Jiang, Heterogeneous iron oxide/dysprosium oxide nanoparticles target liver for precise magnetic resonance imaging of liver fibrosis, ACS Nano 16 (2022) 5647–5659.

[43] A.V. Singh, M.H.D. Ansari, D. Rosenkranz, R.S. Maharjan, F.L. Kriegel, K. Gandhi, A. Kanase, R. Singh, P. Laux, A. Luch, Artificial intelligence and machine learning in computational nanotoxicology: unlocking and empowering nanomedicine, Adv. Healthcare Mater. 9 (2020) 1901862.

[44] O. Adir, M. Poley, G. Chen, S. Froim, N. Krinsky, J. Shklover, J. Shainsky-Roitman, T. Lammers, A. Schroeder, Integrating artificial intelligence and nanotechnology for precision cancer medicine, Adv. Mater. 32 (2020) 1901989.

[45] V. Neuschmelting, H. Lockau, V. Ntziachristos, J. Grimm, M.F. Kircher, Lymph node micrometastases and in-transit metastases from melanoma: in vivo detection with multispectral optoacoustic imaging in a mouse model, Radiology 280 (2016) 137–150.